

Fine-tuning Microporosity of Crystalline Vanadomolybdate Frameworks for Selective Adsorptive Separation of Kr from Xe

Suchona Akter,[†] Yong Li,[†] Minbum Kim,[‡] Md Omar Faruque,[†] Zhonghua Peng,^{*,†} Praveen K. Thallapally,^{*,‡} and Mohammad R. Momeni^{*,†}

[†]*Division of Energy, Matter and Systems, School of Science and Engineering, University of Missouri – Kansas City, Kansas City 64110, MO United States*

[‡]*Physical and Computational Science Directorate, Pacific Northwest National Laboratory, Richland, WA 99352, USA*

E-mail: peng@umkc.edu; praveen.thallapally@pnl.gov; mmomenitaheri@umkc.edu

Abstract: Selective adsorptive capture and separation of chemically inert Kr and Xe noble gases with very low ppmv concentrations in air and industrial off-gases constitute an important technological challenge. Here, using a synergistic combination of experiment and theory, the microporous crystalline vanadomolybdates (MoVO_x) as highly selective Kr sorbents are studied in detail. By varying the Mo/V ratios, we show for the first time that their one-dimensional pores can be fine-tuned for the size-selective adsorption of Kr over the larger Xe with selectivities reaching >100. Using extensive electronic structure calculations and grand canonical Monte-Carlo simulations, the competition between Kr uptake with CO₂ and N₂ was also investigated. As most materials reported so far are selective toward the larger, more polarizable Xe than Kr, this work constitutes an important step toward robust Kr-selective sorbent materials. This work highlights the potential use of porous crystalline transition metal oxides as energy-efficient and selective noble gas capture sorbents for industrial applications.

1. Introduction

Radioactive krypton (Kr) and xenon (Xe) noble gas mixtures produced during the reprocessing of the used nuclear fuel are often responsible for nuclear reactor accidents.¹ ⁸⁵Kr, the most significant radioactive noble gas in the off-gas stream, emits beta (99.6%) and gamma (0.4%) radiations, direct exposure to which harms human health and increases cancer risk.^{2,3} Therefore, the entrapment and separation of these noble gases from off-gas streams are demanded by environmental concerns and are also driven by economic incentives due to the scarcity and high commodity of both Kr and Xe.⁴⁻⁶ For example, Xe is used in healthcare,^{7,8} imaging in the biomedical industry,⁹ and as a satellite propellant in the space industry.¹⁰ Both Kr and Xe are used in lighting,¹¹ lasers,¹² double glazing for insulation,¹³ and as carrier gases in analytical chemistry.¹⁴ This is due to their desirable properties, including high density, low chemical reactivity and solubility, and very low boiling temperature and conductivity.¹⁵ Nevertheless, due to the chemically inert nature of these noble gases, they are difficult to capture and separate. Currently, the only viable option for the separation of Kr and Xe from the spent nuclear fuel is the energy-intensive cryogenic distillation.¹⁶

The Kr/Xe noble gases also possess very low abundances (ppmv level) in air and industrial off-gases, making them even more difficult to capture and separate.¹⁷ Again, the highly energy-intensive cryogenic distillation is the common method for their capture and separation from the at-

mosphere despite their minuscule presence (1.14 and 0.086 ppmv for Kr and Xe, respectively).¹⁸ A more energy-efficient alternative can be physisorption-based separation using microporous materials. Solid adsorbents for capturing noble gases studied so far have been limited to activated carbon,¹⁹ carbon nanotubes (CNTs),^{20,21} zeolites,²² polymers,²³ covalent-organic frameworks (COFs),²⁴ and metal-organic frameworks (MOFs).^{15,25} Despite significant advancements in the development of new adsorbents for the capture and separation of noble gases, the need for novel materials beyond those few studied families is immense. As such, significant research endeavors have recently been devoted to the design and discovery of next-generation solid adsorbents for noble gas separation.²⁶

Given the size and shape of an adsorbent's pores and/or the binding affinity of its adsorption sites, the adsorptive separation of gas mixtures can be realized by differentiating the adsorbate molecular sizes, shapes, polarities, polarizabilities, coordination abilities, and conformations.²⁵ Accordingly, one can classify separation mechanisms as thermodynamic separation, kinetic separation, conformational separation, and molecular sieving. The selectivity, therefore, depends on several factors, such as the adsorbent-adsorbate interactions, the adsorbent's pore size, and the size/shape of the adsorbate molecules.²⁷ Not only a high specific surface area but also pore sizes appropriate to the diameter of one of the components in the gas mixture are crucial for enhanced adsorption capacity. In such a condition, some gas molecules are selectively adsorbed in the pores, while others are excluded (i.e., the size sieving mechanism). Consequently, porous materials with tunable pore sizes and high specific surface areas are highly desirable solid sorbents for the selective adsorptive separation of gas mixtures.^{28,29}

There are currently two key challenges in developing next-generation effective materials for noble gas separation: (i) the demand for structural robustness under different operating conditions, e.g., in radiolytic, corrosive, and chemically reactive environments,³⁰ and (ii) the need for microporous materials with tunable pore sizes given the inert nature of noble gases with negligible charge transfer and polarization effects which limits the separation mechanism to size sieving. Adsorbents based on activated carbon and zeolites have been tested for noble gas capture but have shown low capacity, selectivity, and lack of modularity.³¹⁻³³ From a Kr/Xe separation viewpoint,^{34,35} it is now well-established that (i) selectivity for Xe is maximized in materials with uniform pores slightly larger than Xe (with a kinetic diameter of ≈ 4.1 Å) and (ii) selective Kr capture is achieved in materials with uniform pores smaller than Xe but larger than Kr

(with a kinetic diameter of ≈ 3.7 Å).

In this work, the selective adsorptive separation of Kr over Xe is studied using all inorganic crystalline MoVO_x vanadomolybdate adsorbents via a combination of experimental syntheses and characterizations and theoretical calculations (Figure 1). Crystalline vanadomolybdates MoVO_x are a unique class of intrinsically porous inorganic materials that have been extensively studied for catalytic applications.^{40,74} However, they are yet to be explored as sorbents for Kr/Xe noble gas capture and separation applications. The variability of the fractional occupancy in MoVO_x is a desirable feature of these materials recently utilized to design novel structures with modified Mo/V ratios³⁶ with V centers known to be reduced first.³⁷ A recent XPS analysis has shown that under steady-state conditions, V in these materials remains predominantly in the oxidation state of +4 while Mo adapts an oxidation state of +6.³⁸ In this work, different orthorhombic $\text{Mo}_{40-n}\text{V}_n\text{O}_{112}$ were designed by systematically increasing V contents, resulting in frameworks ranging from $n=0$ (i.e., $\text{Mo}_{40}\text{O}_{112}$ with no V atoms) to $n=16$ where all the linking sites were replaced with V (i.e., $\text{Mo}_{24}\text{V}_{16}\text{O}_{112}$; S1, S2, S3, S4, and S7 sites in Figure 1). Using the obtained lowest energy configurations, the structural, electronic, and Kr/Xe uptakes and selectivities of these materials were studied in detail. Our results show that the introduced changes significantly affect the stability and selectivity of these materials toward Kr/Xe adsorptive separation. Experimental synthesis and characterizations of the representative $\text{Mo}_{30}\text{V}_{10}\text{O}_{112}$ material were also performed, and in agreement with the theory, a higher selectivity toward Kr capture than Xe was obtained. This work is organized as follows: in Section 2, experimental syntheses, characterizations, and adsorption measurements are given; simulation details are outlined in Section 3; results and discussions are presented in Section 4, followed by conclusions and future works.

2. Experimental Section

2.1. Synthesis and Characterization of Crystalline Vanadomolybdate Frameworks

Orthorhombic $\text{Mo}_{30}\text{V}_{10}\text{O}_{112}$ was prepared following a modified literature procedure.³⁹ Ammonium molybdate tetrahydrate $[(\text{NH}_4)_6\text{Mo}_7\text{O}_{24}\cdot 4\text{H}_2\text{O}$; Sigma-Aldrich] (3.7054 g, 3.00 mmol) was dissolved in deionized water (50.4 mL). Vanadium(IV) oxide sulfate hydrate ($\text{VOSO}_4\cdot x\text{H}_2\text{O}$; Sigma-Aldrich) (1.3774 g) was dissolved in deionized water (50.4 mL). The above two solutions were mixed at room temperature and the resulting mixture was stirred for 10 min and then transferred to a 125-mL Teflon liner of a stainless steel autoclave. The reaction mixture was purged with nitrogen for 10 min and then heated at 175 °C for 48 h. After cooling to room temperature, the reaction mixture was then filtered. The obtained solid was washed with deionized water and then dried at 80 °C overnight. A gray solid (1.3970 g) crude product was obtained. The crude solid was added to an aqueous solution of oxalic acid (0.4 M, 35 mL), and this mixture was stirred at 60 °C for 30 min. The mixture was then subjected to vacuum filtration. The solid obtained was washed with deionized water and then dried at 80 °C overnight. The solid was then moved to a conventional furnace and heated at 10 °C.min⁻¹ to 400 °C in air. After calcination at 400 °C for 2 h, a solid product (0.80 g) was obtained. Crystal structure characterization was carried out by X-ray diffraction measurement on a PANalytical Empyrean diffractometer with Cu target at a tube voltage/current of 45

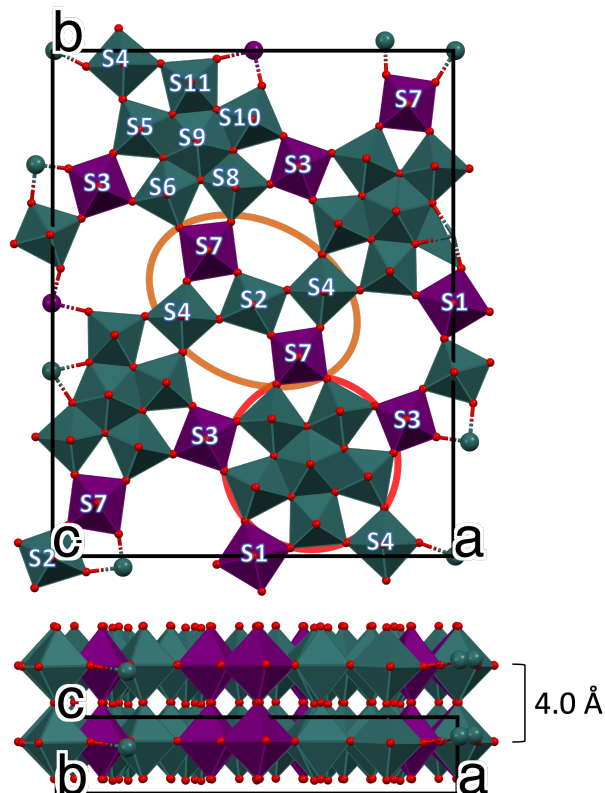


Figure 1. The layered crystal structure of the representative orthorhombic $\text{Mo}_{30}\text{V}_{10}\text{O}_{112}$ vanadomolybdate along the crystallographic “c” (top) and “a” (bottom) axes, respectively. The unit cell contains four hexagonal and four heptagonal pores. The red and orange circles show pentagonal and pentameric units, respectively. The interlayer distance is also given in Å.

kV/40 mA, see Supporting Information (SI) Figure S1. The theta-2theta scan range was performed from 5 to 70 degrees in continuous scan mode. The detector used was a 1D detector (PIXcel) with 255 channels with a step size of 0.01313 degrees. A divergence slit of 1/8 degrees was used to limit the length of the sample illuminated with the incident X-ray beam, whereas an anti-scatter slit of 1/4 degrees was used to reduce the amount of background radiation. The XRD pattern of the final synthesized orthorhombic $\text{Mo}_{30}\text{V}_{10}\text{O}_{112}$ crystals (SI Figure S1) matches very well with those reported in the literature.^{39,40}

2.2. Kr/Xe Adsorption Measurements

The single-component Kr and Xe adsorption isotherms were measured using a 3Flex (Micromeritics instruments, USA). The sample (approx. 100 mg) was activated at 100 °C for 16 h followed by 300 °C for 2 h under vacuum. The first adsorption experiment (1st-Kr, Figure 2), conducted on the activated sample for Kr at 298 K, resulted in a Kr adsorption uptake of approximately 0.24 mmol/g at 1 bar. Subsequently, Kr was desorbed using only vacuum without heating, followed by a second Kr adsorption experiment (2nd-Kr, Figure 2) measured at the same 298 K temperature. In the second Kr adsorption experiment, the sample exhibited a negligible decrease in Kr adsorption at low pressure and nearly identical Kr adsorption uptake at 1 bar. After degassing the sample using a vacuum without heating, a third adsorption experiment (3rd-Xe, Figure 2) was conducted for Xe at 298 K. At 1 bar, the sample exhibited a Xe adsorp-

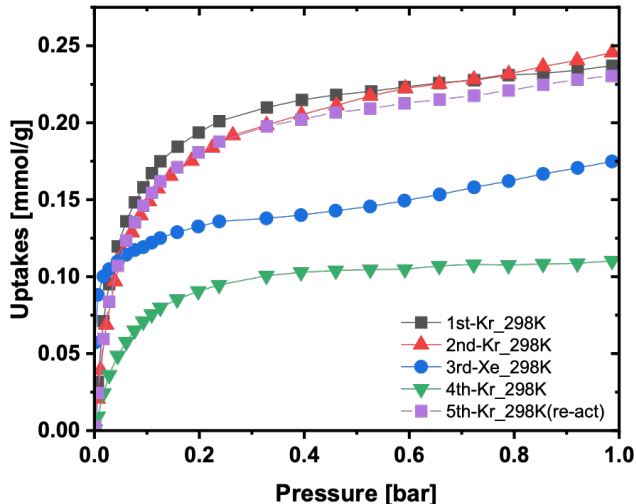


Figure 2. Measured Kr and Xe single-component adsorption isotherms for orthorhombic $\text{Mo}_{30}\text{V}_{10}\text{O}_{112}$ at 298 K. See the text for details.

tion uptake of approximately 0.17 mmol/g, which was lower than the Kr adsorption uptake (0.24 mmol/g). After the Xe adsorption experiment, the sample was degassed with a simple vacuum, and a fourth experiment (4th-Kr, Figure 2) was performed for Kr at 298 K. Interestingly, the sample exhibited a significantly decreased Kr uptake (0.1 mmol/g) compared to the previous Kr uptake (1st and 2nd experiments). The decrease in Kr uptake could be attributed to the Xe molecules partially occupying the sample’s pores, which were not completely desorbed by applying only vacuum without heating. To address the decreased Kr uptake, the sample was re-activated at 100 °C for 2 h. Subsequently, the Kr adsorption was measured again at 298 K (5th-Kr, Figure 2), confirming that the Kr uptake was almost similar to the previous Kr uptake.

3. Theory and Simulation Details

3.1. Electronic Structure Calculations

Comparative adsorptive performance of vanadomolybdate frameworks with different Mo/V ratios has not been reported previously. Here, microporous orthorhombic $\text{Mo}_{40-n}\text{V}_n\text{O}_{112}$ materials with different V contents are considered with $n=0, 2, 4, 6, 8, 10, 12, 14,$ and 16 encompassing $\text{Mo}_{40}\text{O}_{112}$ system with no V atoms, to the V-rich $\text{Mo}_{24}\text{V}_{16}\text{O}_{112}$ system where all the octahedral linking sites are doped with V (see Figure 1). Using our in-house codes, each system was initially created by placing the V atoms on all possible linking sites. The lowest energy configuration was located for all systems by subjecting all isomers to full minimizations using dispersion-corrected density functional theory (DFT) calculations in VASP.^{41–45} Periodic boundary conditions were used in all calculations. For $n=0$ and 16 systems, there is only one possible isomer. The lowest energy isomer for $n=10$, i.e., $\text{Mo}_{30}\text{V}_{10}\text{O}_{112}$, has already been identified and was taken from Ref. 46.

Interactions between electrons and ions were described by Projector Augmented Wave (PAW) potentials^{47–49} with the energy cutoff of 500 eV. Gaussian smearing was adopted in all atomic position and cell vector minimizations with a smearing width of 0.05 eV. The convergence criteria were set to 10^{-5} for SCF and 10^{-6} for electronic property calculations. The k -point mesh in the Monkhorst–Pack⁵⁰ scheme was set to $1 \times 1 \times 6$ in the geometry optimizations and twice

denser for the electronic property calculations. The precision for all calculations was set to “high”, which increases the plane-wave cutoff energy by 30%. The spin polarization of the unpaired electrons was considered with the ISPIN and NUPDOWN parameters in VASP. Different spin states were considered, and the lowest-energy states were identified for all studied systems whenever applicable.

Comprehensive benchmarks were performed for the representative $\text{Mo}_{30}\text{V}_{10}$ system against previously reported⁴⁶ dispersion-corrected hybrid B3LYP-D2 data.^{51,52} These include cutoff energy, k -point mesh, and different GGA functionals, including Perdew-Burke-Ernzerhof (PBE),⁵³ revised PBE (RPBE), PBE for solids (PBEsol),⁵⁴ dispersion-corrected PBE-D2 and PBE-D3,⁵² as well as PBE with Hubbard U correction (PBE-U), with varying U values (see SI Figure S2 and Table S6). The Hubbard-U correction was added for the Mo and V transition metals to compensate for the over-delocalization of d -electrons commonly encountered with GGA functionals, as well as for the p orbitals of the O atoms.⁵⁵ The rotationally invariant Hubbard U parameter, as proposed in Ref. 56, reflects the strength of the on-site Coulomb interactions, whereas the parameter J adjusts the exchange interactions. These two parameters are usually combined into a single parameter $U_{eff}=U-J$. Here, different U_{eff} parameters were benchmarked according to the ranges specified in Ref. 55 and are tabulated in the SI Figure S2. For these benchmarks, different U_{eff} parameters were tested for reproducing the unit cell and atomic positions as reported in Ref. 46. Our extensive benchmarks for the representative $\text{Mo}_{30}\text{V}_{10}$ system showed that the PBE+U method combined with Grimme’s DFT-D3 dispersion correction and Becke-Johnson damping⁵⁷ worked well and closely reproduced that of the reference (see SI Figure S2 and Table S6). This methodology was, therefore, adapted for the remainder of the systems.

Formation energy (ΔE_f) is among the essential descriptors for predicting the thermodynamic stability of an unknown system and is defined as the energy required to form a material from its constituent elements. The formation energies of all considered systems were calculated using the following equation:⁵⁸

$$\Delta E_f = E_{tot} - \sum_i \mu_i x_i \quad (1)$$

where E_{tot} is the DFT calculated total energy of the system, with μ_i being the chemical potential of element i and x_i the quantity of element i in the material. To probe the effects of different Mo/V contents on the structural properties of the lowest energy systems, a variety of geometric features, including density, porosity, gravimetric and volumetric surface areas (GSA and VSA), largest cavity diameter (LCD), and pore limiting diameter (PLD) were calculated using Zeo++.^{59,60} A He probe with a vdW radius of 1.4 Å was used.

3.2. Molecular Simulations

Single-component adsorption isotherms for Kr, Xe, and the competing CO_2 and N_2 adsorbates were calculated at 298 K using Grand Canonical (μ VT ensemble) Monte Carlo (GCMC)³⁴ simulations as implemented in RASPA.^{61,62} The selectivity for Kr capture in 50:50 and 80:20 Kr/Xe mixtures was simulated at 298 K. Equimolar mixtures of Kr with the competing CO_2 and N_2 adsorbates were also simulated using GCMC simulations in RASPA. The universal force field (UFF)^{1,63} was used for all studied vanadomolybdates except

for the O atoms, which was taken from Ref. 64. The rigid framework approximation was used for all studied materials with their atomic positions fixed at their PBE-U-D3(BJ) minimized positions.^{65,66} Peng-Robinson equation of state was used to calculate the relationship between the chemical potential and the pressure of the systems (fugacities). Periodic boundary conditions were employed in all simulations to remove surface effects. An atom-atom cutoff distance of 12.0 Å was employed for truncating the short-range interactions, while long-range electrostatics were calculated using the Ewald summation technique.⁶⁷ Simulations were performed in cells with sufficient repeat units such that all side lengths were greater than 24 Å. Partial atomic charges were calculated using Bader charge analysis with the exception that a charge of zero was assigned to noble gases given their chemically inert nature.⁶⁸ Among the adsorbates, Kr and Xe were modeled using parameters from Ref. 69 and N₂ and CO₂ were modeled using the TraPPE force field.⁷⁰ The 6-12 Lennard-Jones (LJ) potential was employed to describe adsorbent-adsorbate and adsorbate-adsorbate interactions with all cross terms computed using the Lorentz-Berthelot mixing rules. To achieve higher accuracies, the ϵ_{Kr-O} and ϵ_{Xe-O} parameters were adjusted to reproduce our experimental adsorption isotherms (see SI Figure S3). 1×10^6 Monte Carlo equilibration cycles were found to suffice for all systems, whereas 2×10^6 production cycles were used to calculate ensemble averages. Our extensive GCMC benchmarks for all systems are included in SI Figures S4-S20. Four types of Monte Carlo (MC) moves in equal probabilities, including swap (addition/deletion), reinsertion, random rotation, and translation of the adsorbate molecules, were considered for single-component adsorption isotherms. In addition to these MC moves, the identity change probability (e.g., changing Kr to Xe) was also considered in two-component adsorption isotherms. All simulations were performed at 298 K and pressures of 0.02, 0.04, 0.06, 0.08, 0.10, 0.15, 0.20, 0.25, 0.30, 0.35, 0.40, 0.45, 0.50, 0.55, 0.60, 0.65, 0.70, 0.75, 0.80, 0.85, 0.90 and 1.00 bar. The He void fractions for the structures were calculated using widom insertions.⁷¹ All potential parameters are listed in SI Tables S2-S5.

Adsorption selectivity is an important parameter for probing the separation capability of a potential adsorbent material. For the two-component mixtures of Kr and Xe, the selectivity $S_{Kr/Xe}$ was calculated using the following equation:

$$S_{Kr/Xe} = \frac{x_{Kr}/x_{Xe}}{y_{Kr}/y_{Xe}} \quad (2)$$

where x and y are adsorbed gas loadings in the material and mole fraction of adsorbates in bulk, respectively. The same equation was used to calculate the selectivity of Kr and Xe with an equimolar mixture of N₂ and CO₂. As a measure of the adsorbate-adsorbent attraction strengths, the fluctuation method⁷² was used to calculate the isosteric heat of adsorption (Q_{st}) at 1 bar as

$$Q_{st} = \frac{\langle UN \rangle - \langle U \rangle \langle N \rangle}{\langle N^2 \rangle - \langle N \rangle^2} - RT \quad (3)$$

where R , T , U , and N are the universal gas constant, temperature, energy, and number of particles, respectively, with brackets representing ensemble averages.

4. Results and Discussion

4.1. Structural and Thermodynamic Properties of V-Doped Vanadomolybdates

Vanadomolybdate frameworks are known to crystallize in four different phases: orthorhombic, trigonal, tetragonal, and amorphous, each with different porosities and surface areas.⁷³ Out of these, orthorhombic MoVO_x oxides have attracted much attention due to their outstanding catalytic performance, for example, in oxidative activation of short-chain alkanes.^{40,74} Orthorhombic MoVO_x features slabs comprising 1D hexagonal and heptagonal pores of corner-sharing MO₆ octahedra (M = Mo or V) and pentagonal Mo₆O₂₁ units with MoO₇ pentagonal bipyramidal units and five edge-sharing MO₆ octahedra (see Figure 1).^{75,76} Stacking of the six and seven-membered rings constructs 1D channel structures, with the seven-membered channel forming a micropore with a diameter of around 4 Å that allows small molecules such as methane, ethane, N₂, Ar, and CO₂ to enter.⁷⁷ This orthorhombic M1 phase of MoVO_x is known to crystallize in the Pba2 space group which closely resembles that of the so-called M1 phase of MoVTenbO_x.⁷⁸ It shows a characteristic layered structure stacked in the “c” direction (Figure 1). Per unit cell, this microporous material contains two pentameric units, four pentagonal units, and six octahedral linker sites.^{79,80} The space group Pba2 imposes constraints on the M1 MoVO_x structure such that only 11 among the 40 transition metal centers are symmetry inequivalent, labeled as S1, S2, ..., S11 (see Figure 1).⁸⁰

As mentioned above, it has already been established that the stability of the M1 phases of MoVO_x and MoVNbTeO depend on the distribution of the V centers.^{46,81,82} We extensively surveyed V site occupancies in MoVO_x as linker sites in these materials are known to host both Mo and V atoms.⁸³ Initial experiments suggested that, the pentagonal sites S5, S6, S8, S9, S10, and S11 exhibit the highest occupancy for Mo followed by the linking S2, S4, S3, S7, and S1 sites, with the order S9≈S5≈S6>S8≈S10≈S11>S2>S4≈S3≈S7>S1.^{84,85} These preliminary results were first deduced based on powder diffraction data, but later on, scanning transmission electron microscopy (STEM) data generated a more accurate occupancy scenario for similar systems.³⁶ For example, it was demonstrated that all octahedra sites connecting the pentagonal units (S1, S2, S3, and S4, Figure 1) contain appreciable amounts of V.^{79,86} The S5, S6, and S11 sites were also found to contain about 5, 12, and 5% V, respectively, but the sites S8 and S10 were shown to contain only Mo. The V atoms were found to strongly prefer the corner-sharing octahedra rather than the edge-sharing sites. Later experiments reported that the highest V occupancies belong to the S1, S3, and S7 sites,⁸⁷ with S4 being a highly Mo-dominant site with Mo occupancies close to 100%.⁸¹

Guided by these results, a full survey of all possible V-doped structures was performed for the extended family of the vanadomolybdate MoVO_x materials using dispersion-corrected PBE-U-D3 calculations in VASP. The presence of V atom in the S4 sites was found to always result in relatively high energy isomers, which agrees with the experimental observation of significantly lower V occupancy in S4 sites for the M1 orthorhombic phase of vanadomolybdates as well as for the MoVTeO and MoVTenbO materials mentioned above.^{86,87} The lowest energy isomer for Mo₃₀V₁₀ contains V in S1, S3, and S7 sites with the ordering of S1 > S3 > S7, which also agrees with experiment.⁸¹ In the lowest energy isomer of Mo₂₈V₁₂, S1, S2, S3, and S7 sites are occupied by V. There is no V in any of the four S4 sites in the unit cell.

Figure 3 shows the calculated formation energy increases

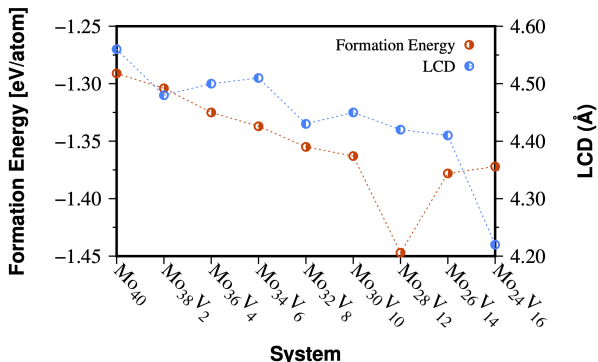


Figure 3. Calculated (a) formation energies (in eV/atom) and (b) LCD (in Å) of all systems considered in this work.

(i.e., becomes more negative) as the V content increases up to $n = 14$, and then plateaus at $n = 16$ with the $\text{Mo}_{28}\text{V}_{12}$ system being an outlier with the lowest calculated formation energy of -1.447 eV/atom. Our computed trend of formation energies here overall agrees very well with Ref. 82, where for the similar M1 phase of MoVNbTeO , DFT calculations showed that the structure stabilizes by increasing the concentration of V. Interestingly, as for the $\text{Mo}_{28}\text{V}_{12}$ with the lowest calculated formation energy, we found that its unit cell volume is also the highest among all studied systems. This increased volume is resulted from an elongated “c” axis in this material compared to the others. We attribute this rather significant unit cell change in $\text{Mo}_{28}\text{V}_{12}$ to the Jahn-Teller (JT) effect,⁸⁸ most commonly observed in octahedral transition metal complexes.⁸⁹ According to the JT effect, a distortion happens in nonlinear complexes, splitting the degenerate energy levels and lowering the overall symmetry, which results in higher stabilities.⁸⁸ As a result, the average VO_6 octahedra length is the highest (4.3 Å) for $\text{Mo}_{28}\text{V}_{12}$, whereas for the other systems it ranges from 3.9 Å in $\text{Mo}_{26}\text{V}_{14}$ to 4.1 Å in Mo_{36}V_4 . For all studied systems, one can see a conspicuous trend in their calculated geometric parameters with an increase in the V content. Specifically, the calculated LCD, PLD, GSA, and VSA are the highest for Mo_{40} with no V and the lowest for the V-rich $\text{Mo}_{24}\text{V}_{16}$ system (see SI Table S7). This is due to the smaller ionic radius of V compared to that of Mo (0.54 Å for V^{+5} vs. 0.59 Å for Mo^{+6}), resulting in slightly smaller pore sizes as more Mo atoms are replaced with V. As such, the expectation for these materials is for them to become more selective toward the smaller Kr than Xe as the pore sizes are reduced upon V doping. More specifically, $\text{Mo}_{24}\text{V}_{16}$ with a computed LCD of 4.22 Å is expected to effectively exclude the larger Xe atoms with a kinetic diameter of ≈ 4.1 Å compared to Mo_{40} with the calculated largest LCD value of 4.56 Å. Kr/Xe adsorption and selectivity and their possible correlations with these geometric features are outlined in detail in the next section.

4.2. Kr/Xe Adsorption in V-Doped Vanadomolybdates

Single-component adsorption isotherms of Kr and Xe were calculated using GCMC simulations at 298 K in RASPA (Figure 4). Overall, increasing the V content in the studied MoVO_x vanadomolybdates was found to lower the uptake for both Kr and Xe. This is consistent with the computed decreasing trend in the calculated surface area and porosity of these materials as more Mo ions are replaced by the smaller V ones. Interestingly, the Xe uptake, which is ini-

tially higher than Kr for $n = 0$ and 2, was found to become similar at the higher 1 bar pressure for $n = 4$ in the Mo_{36}V_4 system. And, starting from Mo_{34}V_6 , the order was calculated to reverse with Kr uptake becoming higher than Xe. The Xe uptake was found to continuously go down as more V atoms are introduced to the material till for $\text{Mo}_{24}\text{V}_{16}$, where the material can virtually no longer adsorb Xe.

The isosteric heat of adsorption (Q_{st}) of both Kr and Xe were calculated at 1 bar, the results of which are given in Figure 5. The Q_{st} for Kr is calculated to stay almost constant throughout the considered systems (ranging from 31.7 to 27.2 kJ/mol), whereas for Xe, it starts off from 39.2 kJ/mol for Mo_{40} and continuously goes down and plateaus at $\text{Mo}_{26}\text{V}_{14}$ and then sharply decreases to 20.0 kJ/mol for $\text{Mo}_{24}\text{V}_{16}$ (Figure 5 and SI Table S8). This calculated trend for Xe can be easily understood based on its larger kinetic diameter of ≈ 4.1 Å compared to that of ≈ 3.7 Å for Kr. As mentioned above, V doping leads to overall lower pore sizes as the ionic radius of the V atoms is smaller than that of Mo. As a result, the heptagonal pores continuously shrink as V content increases with the material ultimately being able to effectively exclude the larger Xe atoms. Our higher calculated Q_{st} value for Xe than Kr in the case of $\text{Mo}_{30}\text{V}_{10}$ (32.2 vs. 30.2 kJ/mol, SI Table S8) agrees qualitatively with our experimental characterizations that applying heat is necessary in order to evacuate the adsorbed Xe from the micropores of this material (see Figure 2). Since V-doping leads to higher stabilities, as judged by the calculated formation energy trends (Figure 3), the V-rich vanadomolybdates are expected to be viable candidates for synthesis and characterization.

As demonstrated in Figure 6a, Kr selectivity is found to increase with an increase in V doping, with $\text{Mo}_{24}\text{V}_{16}$ being the highest Kr selective material with a calculated selectivity of 106.5 for an equimolar Kr/Xe mixture (SI Table S7). Moreover, $\text{Mo}_{26}\text{V}_{14}$ and $\text{Mo}_{28}\text{V}_{12}$ show around six times more Kr selectivity than Xe, with $\text{Mo}_{30}\text{V}_{10}$ and Mo_{32}V_8 showing a Kr/Xe selectivity of around two. The rest of the systems show more selectivity towards Xe, with the highest Xe selectivity in Mo_{40} . By far, MOFs are the most studied materials for Kr and Xe adsorption separation. However, most reported MOFs are exclusively Xe selective.^{90–92} For example, SBMOF-1 exhibits a high Xe adsorption of 13.2 mmol/kg and an Xe/Kr selectivity of 16.⁹³ Z11CBF-1000-2 is another MOF with a 20.6 mmol/kg uptake capacity for Xe and an Xe/Kr selectivity of 19.7.⁹⁴ JAVTAC and KAXQIL are another two examples with high Xe adsorption as well.³⁵ As for Kr selective materials, FMOF-Cu was the first reported material with a high Kr/Xe selectivity of 36, at 203 K and 0.1 bar.⁹⁵ In addition, UTSA-280 and CECYOY are two theoretically predicted materials with Kr uptakes of 1.48 and 0.23 mmol/g, respectively, and Kr/Xe selectivity of 72.1 and 248.3, respectively.^{1,96} Overall, based on selectivity for Kr/Xe adsorption, we have found that the $\text{Mo}_{24}\text{V}_{16}$ (106.5), $\text{Mo}_{26}\text{V}_{14}$ (6.7) and $\text{Mo}_{28}\text{V}_{12}$ (5.4) are among the top performing materials for Kr selective adsorptive separation.

Expectedly, the calculated Kr/Xe selectivity was found to correlate well with the calculated LCDs (see Figure 6b). As mentioned previously, doping with more V incrementally decreases the calculated LCDs, subsequently making the Xe adsorption more unfavorable compared to that of the smaller Kr. As discussed above, this is consistent with the molecular sieving mechanism for Kr/Xe adsorptive separation in these materials. Calculated radial distribution functions (RDFs)

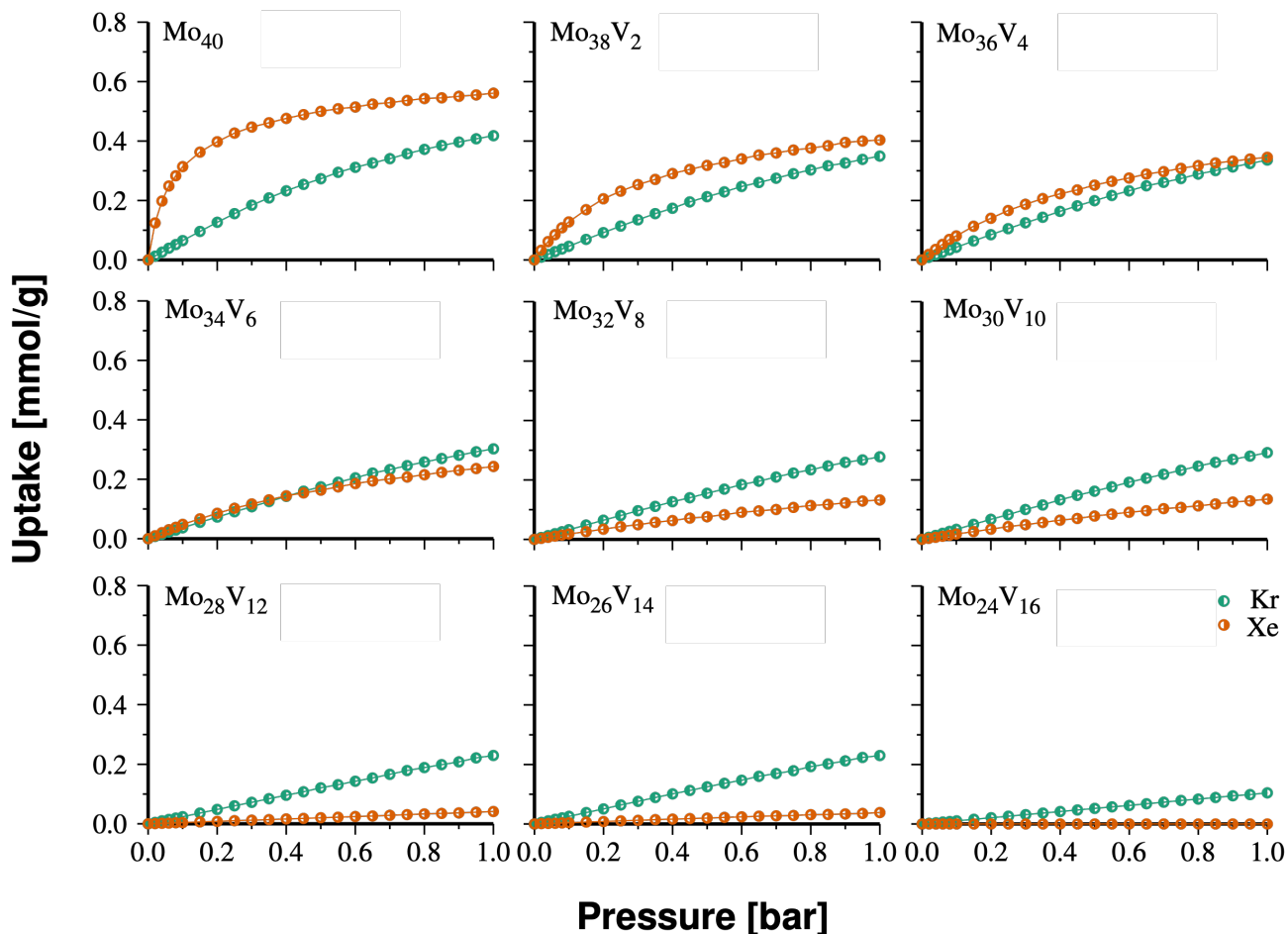


Figure 4. GCMC calculated Kr and Xe single-component adsorption isotherms of all considered systems at 298 K using RASPA.

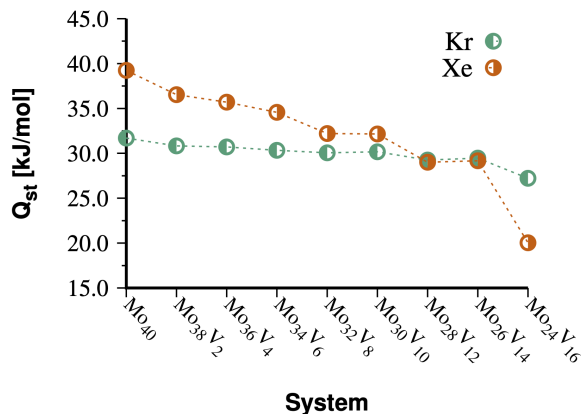


Figure 5. GCMC calculated Q_{st} for Kr and Xe at 298 K and 1 bar for all systems considered in this work.

for the distances between the O atoms of different solid sorbents and Kr and Xe adsorbates are given in the SI Figure S24. The calculated Kr-O distances were found to be uniform and relatively constant, centered around ≈ 3.8 Å, for all studied materials, whereas a rather large range of 3.6 Å–4.2 Å was found for Xe-O distances (SI Figure S24).

Figure 7 shows the calculated Pearson correlation matrix across different features of the studied materials. As discussed, a good correlation exists between calculated selec-

tivity from GCMC simulations and LCD from Zeo++ that can be used for high-throughput screening purposes, bypassing the need for expensive GCMC simulations. They could also be used as useful features in developing machine learning models, which are currently under investigation in our labs.

4.3. Competition with CO₂ and N₂

CO₂ and N₂ molecules are abundant in air and can therefore compete with Kr uptake. Subsequently, pure component adsorption isotherms for the competing CO₂ and N₂ molecules were calculated at 298 K for all considered systems (see SI Figure S25). The CO₂ uptake was found not to follow the computed trend for LCDs and instead to be similar for all systems except for Mo₂₄V₁₆ and Mo₂₈V₁₂, which are about half compared to the rest. Instead for N₂, except Mo₃₀V₁₀, the adsorption was found to follow the trend for calculated LCDs with Mo₄₀ and Mo₂₄V₁₆ showing the highest and lowest uptakes, respectively. To rationalize these trends and outliers, we first note that in contrast to the studied Kr and Xe noble gasses with zero assigned charges, both CO₂ and N₂ carry charges, and therefore, electrostatic interactions might play a major role. To further investigate this, the calculated Bader charges of all systems were analyzed (see SI Table S5). The calculated average charges of the framework O atoms were found to be the highest for the Mo₃₀V₁₀ system. On the other hand, Mo₂₈V₁₂ and Mo₂₄V₁₆ were found to have the lowest charges for these O atoms. As such, compared to the rest of the studied systems, electrostatic interactions

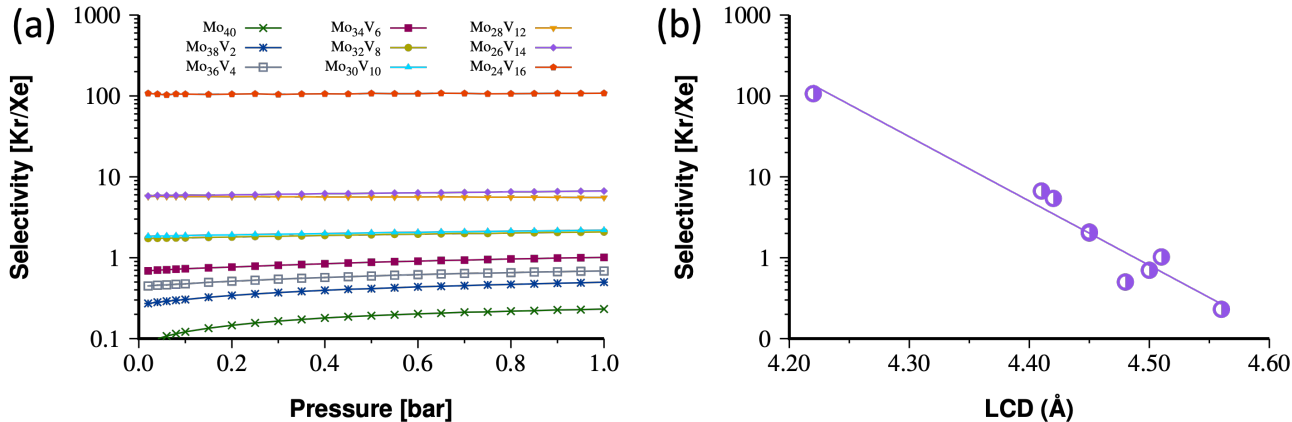


Figure 6. GCMC calculated (a) Kr/Xe selectivity for the 50:50 mixture at 298 K and (b) correlation ($R^2 = 0.81$) between Kr/Xe selectivity (logarithmic scale) for the 50:50 mixture and LCD. A line is added to guide the eye. The corresponding data for the 80:20 mixture is given in the SI Figure S21.

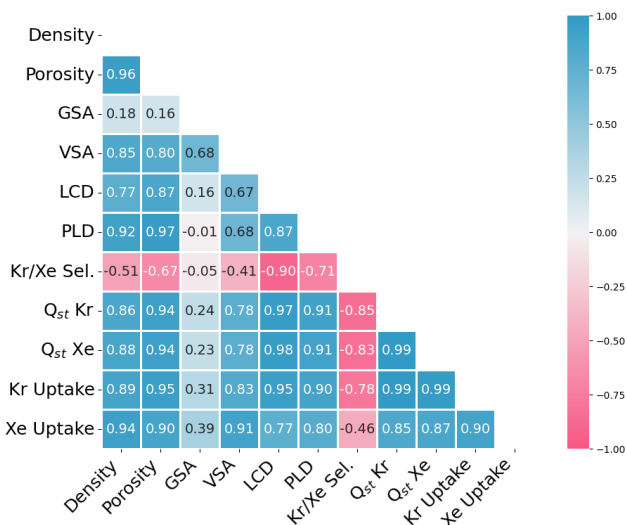


Figure 7. The Pearson correlation coefficient matrix for all systems studied in this work.

are anticipated to be stronger between N₂ and Mo₃₀V₁₀ but weaker for CO₂ interactions with Mo₂₈V₁₂ and Mo₂₄V₁₆.

To study the competition between Kr uptake in the presence of the competing CO₂ and N₂ adsorbates, the selectivity of all studied systems for binary equimolar mixtures of Kr/CO₂ and Kr/N₂ was calculated. We note that as the main focus of this work is to develop materials with high Kr selectivity, we focus here only on Kr selectivity in the presence of these competing adsorbates. As shown in the SI Figure S25, except Mo₃₀V₁₀, all considered materials exhibit higher selectivity toward Kr adsorption than N₂ (see our rationale for Mo₃₀V₁₀ above). In agreement with their calculated CO₂ uptakes, the Mo₂₈V₁₂ and Mo₂₄V₁₆ systems were found to be the least CO₂ selective materials followed by Mo₃₀V₁₀ compared to the rest of the considered systems. Overall, none of the studied systems was found to be more selective towards Kr than CO₂. This implies that CO₂ could potentially compete with Kr adsorption and should, therefore, be removed from the mixture before these materials can be used for separating Kr.

As mentioned before, the studied orthorhombic vanadomolybdates contain four heptagonal and four hexagonal

pores in their unit cells. Given the kinetic diameters of Kr and Xe and the calculated PLDs (ranging from 3.05 Å to 3.43 Å) and LCDs (ranging from 4.22 Å to 4.56 Å) for the hexagonal and heptagonal pores, respectively, the adsorption was found to only occur in the larger heptagonal channels. To further confirm this, Kr/Xe uptakes were calculated after blocking the heptagonal pores, which led to zero uptakes not only for Kr and Xe but also for the competing CO₂ and N₂ adsorbates. On the other hand, when the hexagonal pores were blocked, adsorption isotherms similar to those of the unblocked simulations were obtained (see the calculated Kr and Xe density distribution plots in SI Figure S26).

5. Conclusion

Extensive electronic structure calculations and molecular simulations combined with targeted synthesis and characterizations are used to explore vanadium doping as an effective tool for fine-tuning the microporosity of an underexplored family of mixed metal oxide vanadomolybdates for selective Kr uptake from Kr/Xe mixtures in the presence of other competing CO₂ and N₂ adsorbates. Unprecedented Kr selectivities as high as >100 were found by effective size exclusion of the larger Xe adsorbates in V-rich materials. Useful correlations were found between Kr/Xe uptakes and selectivity and LCD, porosity, and isosteric heat of adsorption. These correlations are very useful as excellent features for training machine learning models or fast high-throughput screening of these materials. One possibility to increase Kr uptake is to explore other phases of vanadomolybdates, such as the trigonal phase, which has already been synthesized and used for catalytic oxidation purposes. This trigonal phase contains a higher heptagonal/hexagonal ratio of 3/2, compared to that of 1/1 for the studied orthorhombic vanadomolybdates in this work. This should lead to higher Kr uptakes in the former, considering similar levels of V-doping. We hope that this study is helpful in providing useful insights into a new class of chemically robust all-inorganic materials for selective Kr adsorptive separation under extreme operating conditions.

Supporting Information Available

Benchmark of our electronic structure calculations, force field parameters used in RASPA simulations, convergence tests using different number of cycles for GCMC simulations, and simulated uptakes and selectivities for CO₂ and N₂.

Acknowledgement This work is partially supported by the U.S. Department of Energy Office of Science, Basic Energy Sciences Program (Grant No. DE-SC0024512). PKT thanks DOE Nuclear Energy – Materials Research and Waste Form Development Campaign. Particularly, PKT thanks Dr. Ken Marsden (INL), Mrs. Amy Welty (INL), and Mrs. Kimberly Gray (DOE Nuclear Energy). ZP and MRM thank UMKC Tier 1 Funding For Excellence (FFE) grant for support. We thank Dr. James B. Murowchick of UMKC for his assistance in powder X-ray measurements. Simulations presented in this work used resources from Bridges-2 at Pittsburgh Supercomputing Center through allocation PHY230099 from the Advanced Cyberinfrastructure Coordination Ecosystem: Services & Support (ACCESS) program,⁹⁷ which is supported by National Science Foundation grants #2138259, #2138286, #2138307, #2137603, and #2138296. Technical support and computing resources provided by the HPC center at UMKC are also gratefully acknowledged.

References

- (1) Lin, W.-q.; Xiong, X.-l.; Liang, H.; Chen, G.-h. Multiscale Computational Screening of Metal-Organic Frameworks for Kr/Xe Adsorption Separation: A Structure-Property Relationship-Based Screening Strategy. *ACS Appl. Mater. Interfaces* **2021**, *13*, 17998–18009.
- (2) Abe, K.; Hosaka, J.; Iida, T.; Ikeda, M.; Kobayashi, K.; Koshio, Y.; Minamino, A.; Miura, M.; Moriyama, S.; Nakahata, M.; Nakajima, Y.; Namba, T.; Ogawa, H.; Sekiya, H.; Shiozawa, M.; Suzuki, Y.; Takeda, A.; Takeuchi, Y.; Ueshima, K.; Yamashita, M.; Kaneyuki, K.; Ebizuka, Y.; Kikuchi, J.; Ota, A.; Suzuki, S.; Takahashi, T.; Hagiwara, H.; Kamei, T.; Miyamoto, K.; Nagase, T.; Nakamura, S.; Ozaki, Y.; Sato, T.; Fukuda, Y.; Sato, T.; Nishijima, K.; Sakurai, M.; Maruyama, T.; Motoki, D.; Itow, Y.; Ohsumi, H.; Tasaka, S.; Kim, S.; Kim, Y.; Lee, J.; Moon, S.; Urakawa, Y.; Uchino, M.; Kamioka, Y. Distillation of Liquid Xenon to Remove Krypton. *Astrophys. J.* **2009**, *31*, 290–296.
- (3) *Krypton-85 in the atmosphere: accumulation, biological significance, and control technology*; 1975; National Council on Radiation Protection and Measurements, Washington, DC (USA).
- (4) Sunder, S.; Shoesmith, D.; Kolar, M.; Leneveu, D. Calculation of Used Nuclear Fuel Dissolution Rates Under Anticipated Canadian Waste Vault Conditions. *J. Nucl. Mater.* **1997**, *250*, 118–130.
- (5) Liu, L. T.; Xu, Y.; Tang, P. Mechanistic Insights Into Xenon Inhibition of NMDA Receptors From MD Simulations. *J. Phys. Chem. B* **2010**, *114*, 9010–9016.
- (6) Feng, X.; Zong, Z.; Elsaïdi, S. K.; Jasinski, J. B.; Krishna, R.; Thallapally, P. K.; Carreon, M. A. Kr/Xe Separation Over a Chabazite Zeolite Membrane. *J. Am. Chem. Soc.* **2016**, *138*, 9791–9794.
- (7) Cullen, S. C.; Gross, E. G. The Anesthetic Properties of Xenon in Animals and Human Beings, with Additional Observations on Krypton. *Science* **1951**, *113*, 580–582.
- (8) Sanders, R. D.; Ma, D.; Maze, M. Xenon: Elemental Anaesthesia in Clinical Practice. *Br. Med. Bull.* **2005**, *71*, 115–135.
- (9) Albert, M.; Cates, G.; Driehuys, B.; Happer, W.; Saam, B.; Springer Jr, C.; Wishnia, A. Biological Magnetic Resonance Imaging Using Laser-Polarized ¹²⁹Xe. *Nature* **1994**, *370*, 199–201.
- (10) Beattie, J.; Matossian, J.; Poeschel, R.; Rogers, W.; Martinelli, R. Xenon Ion Propulsion Subsystem. *J. Propuls. Power* **1989**, *5*, 438–444.
- (11) Yeralan, S.; Doughy, D.; Blondia, R.; Hamburger, R. Advantages of using high-pressure short-arc xenon lamps for display systems. *Projection Displays XI*. 2005; pp 27–35.
- (12) Bridges, W. B.; Chester, A. N. Visible and UV Laser Oscillation at 118 Wavelengths in Ionized Neon, Argon, Krypton, Xenon, Oxygen, and Other Gases. *Appl. Opt.* **1965**, *4*, 573–580.
- (13) Manz, H. On Minimizing Heat Transport in Architectural Glazing. *Renew. Energy* **2008**, *33*, 119–128.
- (14) Lipsky, S.; Shahin, M. Use of Xenon and Krypton as Carrier Gases for a Highly Sensitive Detection System for Gas Chromatography. *Nature* **1963**, *200*, 566–567.
- (15) Banerjee, D.; Simon, C. M.; Elsaïdi, S. K.; Haranczyk, M.; Thallapally, P. K. Xenon Gas Separation and Storage Using Metal-Organic Frameworks. *Chem* **2018**, *4*, 466–494.
- (16) Zhao, G.; Chen, Y.; Chung, Y. G. High-Throughput, Multiscale Computational Screening of Metal-Organic Frameworks for Xe/Kr Separation with Machine-Learned Parameters. *Ind. Eng. Chem. Res.* **2023**, *62*, 15176–15189.
- (17) Wei, Y.; Qi, F.; Li, Y.; Min, X.; Wang, Q.; Hu, J.; Sun, T. Efficient Xe Selective Separation From Xe/Kr/N₂ Mixtures Over a Microporous CALF-20 Framework. *RSC Adv.* **2022**, *12*, 18224–18231.
- (18) Kerry, F. G. *Industrial gas handbook: gas separation and purification*; CRC press, 2007.
- (19) Marsh, H.; Reinoso, F. R. *Activated carbon*; Elsevier, 2006.
- (20) Majumdar, S.; Maurya, M.; Singh, J. K. Adsorptive Separation of CO₂ From Multicomponent Mixtures of Flue Gas in Carbon Nanotube Arrays: A Grand Canonical Monte Carlo Study. *Energ. Fuel* **2018**, *32*, 6090–6097.
- (21) Yang, Y.-B.; Hao, Q.; Müller-Plathe, F.; Böhm, M. C. Monte Carlo Simulations of SO₂, H₂S, and CO₂ Adsorption in Charged Single-Walled Carbon Nanotube Arrays. *J. Phys. Chem. C* **2020**, *124*, 5838–5852.
- (22) Smit, B.; Maesen, T. L. Molecular Simulations of Zeolites: Adsorption, Diffusion, and Shape Selectivity. *Chem. Rev.* **2008**, *108*, 4125–4184.
- (23) Hong, H.; Guo, Z.; Yan, D.; Zhan, H. A Tröger’s Base-Derived Microporous Organic Polymers Containing Pyrene Units for Selective Adsorption of CO₂ Over N₂ and CH₄. *Microporous Mesoporous Mater.* **2020**, *294*, 109870.
- (24) Waller, P. J.; Gándara, F.; Yaghi, O. M. Chemistry of Covalent Organic Frameworks. *Acc. Chem. Res.* **2015**, *48*, 3053–3063.
- (25) Li, J.-R.; Kuppler, R. J.; Zhou, H.-C. Selective Gas Adsorption and Separation in Metal-Organic Frameworks. *Chem. Soc. Rev.* **2009**, *38*, 1477–1504.
- (26) Moyer, B. A.; Lumetta, G. J.; Bruffey, S. H.; Finkeldei, S.; Marsden, K. C.; Simpson, M. F.; Jensen, M. P.; Zalupski, P. R.; Clark, A. E.; Yang, P.; Horne, G. P. Innovative Separations Research and Development Needs for Advanced Fuel Cycles. **2022**.
- (27) Gu, C.; Gao, G.-H.; Yu, Y.-X.; Nitta, T. Simulation for Separation of Hydrogen and Carbon Monoxide by Adsorption on Single-Walled Carbon Nanotubes. *Fluid Ph. Equilib.* **2002**, *194*, 297–307.
- (28) Sun, P.; Wang, K.; Zhu, H. Recent Developments in Graphene-Based Membranes: Structure, Mass-Transport Mechanism and Potential Applications. *Adv. Mater.* **2016**, *28*, 2287–2310.
- (29) Gadipelli, S.; Guo, Z. X. Graphene-Based Materials: Synthesis and Gas Sorption, Storage and Separation. *Prog. Mater. Sci.* **2015**, *69*, 1–60.
- (30) Moyer, B. A.; Lumetta, G. J.; Bruffey, S. H.; Finkeldei, S.; Marsden, K. C.; Simpson, M. F.; Jensen, M. P.; Zalupski, P. R.; Clark, A. E.; Yang, P.; Horne, G. P. *Innovative Separations Research and Development Needs for Advanced Fuel Cycles*; 2022.
- (31) Thallapally, P. K.; Grate, J. W.; Motkuri, R. K. Facile Xenon Capture and Release at Room Temperature Using a Metal-Organic Framework: a Comparison with Activated Charcoal. *Chem. Commun.* **2012**, *48*, 347–349.
- (32) Bazan, R.; Bastos-Neto, M.; Moeller, A.; Dreisbach, F.; Staudt, R. Adsorption Equilibria of O₂, Ar, Kr and Xe on Activated Carbon and Zeolites: Single Component and Mixture Data. *Adsorption* **2011**, *17*, 371–383.
- (33) Jameson, C. J.; Jameson, A. K.; Lim, H.-M. Competitive Adsorption of Xenon and Krypton in Zeolite Na A: ¹²⁹Xe Nuclear Magnetic Resonance Studies and Grand Canonical Monte Carlo Simulations. *J. Chem. Phys.* **1997**, *107*, 4364–4372.
- (34) Sikora, B. J.; Wilmer, C. E.; Greenfield, M. L.; Snurr, R. Q. Thermodynamic Analysis of Xe/Kr Selectivity in Over 137000 Hypothetical Metal-Organic Frameworks. *Chem. Sci.* **2012**, *3*, 2217–2223.
- (35) Simon, C. M.; Mercado, R.; Schnell, S. K.; Smit, B.; Haranczyk, M. What Are the Best Materials to Separate a Xenon/krypton Mixture? *Chem. Mater.* **2015**, *27*, 4459–4475.
- (36) Pyrz, W. D.; Blom, D. A.; Sadakane, M.; Kodato, K.; Ueda, W.; Vogt, T.; Buttrey, D. J. Atomic-Scale Investigation of Two-Component MoVO Complex Oxide Catalysts Using Aberration-Corrected High-Angle Annular Dark-Field Imaging. *Chem. Mater.* **2010**, *22*, 2033–2040.
- (37) López, X.; de Graaf, C.; Maestre, J. M.; Bénard, M.; Rohmer, M.-M.; Bo, C.; Poblet, J. M. Highly Reduced Polyoxometalates: Ab Initio and DFT Study of [PMo₅V₄O₄₀ (VO)₄]⁵⁻. *J. Chem. Theory Comput.* **2005**, *1*, 856–861.
- (38) Andrushkevich, T. Heterogeneous Catalytic Oxidation of Acrolein to Acrylic Acid: Mechanism and Catalysts. *Catalysis Review—Science and Engineering* **1993**, *35*, 213–259.
- (39) Sadakane, M.; Kodato, K.; Kuranishi, T.; Nodasaka, Y.; Sugawara, K.; Sakaguchi, N.; Nagai, T.; Matsui, Y.; Ueda, W. Molybdenum–Vanadium-Based Molecular Sieves with

- Microchannels of Seven-Membered Rings of Corner-Sharing Metal Oxide Octahedra. *Angew. Chem. Int. Ed.* **2008**, *47*, 2493–2496.
- (40) Konya, T.; Katou, T.; Murayama, T.; Ishikawa, S.; Sadakane, M.; Buttrey, D.; Ueda, W. An Orthorhombic Mo₃VO_x Catalyst Most Active for Oxidative Dehydrogenation of Ethane Among Related Complex Metal Oxides. *Catal. Sci. Technol.* **2013**, *3*, 380–387.
- (41) Kresse, G.; Hafner, J. Ab Initio Molecular Dynamics for Liquid Metals. *Phys. Rev. B* **1993**, *47*, 558–561.
- (42) Kresse, G.; Hafner, J. Ab Initio Molecular-Dynamics Simulation of the Liquid-Metal–Amorphous-Semiconductor Transition in Germanium. *Phys. Rev. B* **1994**, *49*, 14251–14269.
- (43) Kresse, G.; Furthmüller, J. Efficiency of Ab-Initio Total Energy Calculations for Metals and Semiconductors Using a Plane-Wave Basis Set. *Comput. Mater. Sci.* **1996**, *6*, 15–50.
- (44) Kresse, G.; Furthmüller, J. Efficient Iterative Schemes for Ab Initio Total-Energy Calculations Using a Plane-Wave Basis Set. *Phys. Rev. B* **1996**, *54*, 11169–11186.
- (45) Kresse, G.; Furthmüller, J. Efficient Iterative Schemes for Ab Initio Total-Energy Calculations Using a Plane-Wave Basis Set. *Phys. Rev. B* **1996**, *54*, 11169.
- (46) Li, W.; Fjermestad, T.; Genest, A.; Roesch, N. How the Distribution of Reduced Vanadium Centers Affects Structure and Stability of the MoVO_x Material. *Catal. Sci. Technol.* **2018**, *8*, 2654–2660.
- (47) Blöchl, P. E. Projector Augmented-Wave Method. *Phys. Rev. B* **1994**, *50*, 17953–17979.
- (48) Kresse, G.; Joubert, D. From ultrasoft pseudopotentials to the projector augmented-wave method. *Phys. Rev. B* **1999**, *59*, 1758–1775.
- (49) Blöchl, P. E. Projector Augmented-Wave Method. *Phys. Rev. B* **1994**, *50*, 17953.
- (50) Monkhorst, H. J.; Pack, J. D. Special Points for Brillouin-Zone Integrations. *Phys. Rev. B* **1976**, *13*, 5188.
- (51) Becke, A. D. Density-functional Thermochemistry. III. The Role of Exact Exchange. *J. Chem. Phys.* **1993**, *98*, 5648–5652.
- (52) Grimme, S.; Antony, J.; Ehrlich, S.; Krieg, H. A Consistent and Accurate Ab Initio Parametrization of Density Functional Dispersion Correction (DFT-D) for the 94 Elements H–Pu. *J. Chem. Phys.* **2010**, *132*.
- (53) Perdew, J. P.; Burke, K.; Ernzerhof, M. Generalized Gradient Approximation Made Simple. *Phys. Rev. Lett.* **1996**, *77*, 3865.
- (54) Perdew, J. P.; Ruzsinszky, A.; Csonka, G. I.; Vydrov, O. A.; Scuseria, G. E.; Constantin, L. A.; Zhou, X.; Burke, K. Restoring the Density-Gradient Expansion for Exchange in Solids and Surfaces. *Phys. Rev. Lett.* **2008**, *100*, 136406.
- (55) Moore, G. C.; Horton, M. K.; Linscott, E.; Ganose, A. M.; Siron, M.; O'Regan, D. D.; Persson, K. A. High-Throughput Determination of Hubbard U and Hund J Values for Transition Metal Oxides Via the Linear Response Formalism. *Phys. Rev. Mater.* **2024**, *8*, 014409.
- (56) Dudarev, S. L.; Botton, G. A.; Savrasov, S. Y.; Humphreys, C.; Sutton, A. P. Electron-Energy-Loss Spectra and the Structural Stability of Nickel Oxide: An LSDA+U Study. *Phys. Rev. B* **1998**, *57*, 1505.
- (57) Johnson, E. R.; Becke, A. D. A Post-Hartree-Fock Model of Intermolecular Interactions: Inclusion of Higher-Order Corrections. *J. Chem. Phys.* **2006**, *124*.
- (58) Kirklin, S.; Saal, J. E.; Meredig, B.; Thompson, A.; Doak, J. W.; Aykol, M.; Rühl, S.; Wolverton, C. The Open Quantum Materials Database (OQMD): Assessing the Accuracy of DFT Formation Energies. *Npj Comput. Mater.* **2015**, *1*, 1–15.
- (59) Willems, T. F.; Rycroft, C. H.; Kazi, M.; Meza, J. C.; Haracz, M. Algorithms and Tools for High-Throughput Geometry-Based Analysis of Crystalline Porous Materials. *Microporous Mesoporous Mater.* **2012**, *149*, 134–141.
- (60) Martin, R. L.; Smit, B.; Haracz, M. Addressing Challenges of Identifying Geometrically Diverse Sets of Crystalline Porous Materials. *J. Chem. Inf. Model.* **2012**, *52*, 308–318.
- (61) Dubbeldam, D.; Calero, S.; Ellis, D. E.; Snurr, R. Q. RASPA: Molecular Simulation Software for Adsorption and Diffusion in Flexible Nanoporous Materials. *Mol. Simul.* **2016**, *42*, 81–101.
- (62) Dubbeldam, D.; Calero, S.; Vlucht, T. J. IRASPA: GPU-Accelerated Visualization Software for Materials Scientists. *Mol. Simul.* **2018**, *44*, 653–676.
- (63) Casewit, C.; Colwell, K.; Rappe, A. Application of a Universal Force Field to Main Group Compounds. *J. Am. Chem. Soc.* **1992**, *114*, 10046–10053.
- (64) Cuadros, F.; Cachadina, I.; Ahumada, W. Determination of Lennard-Jones Interaction Parameters Using a New Procedure. *Mol. Eng.* **1996**, *6*, 319–325.
- (65) Ozturk, Z.; Baykasoglu, C.; Celebi, A. T.; Kirca, M.; Mugan, A.; To, A. C. Hydrogen Storage in Heat Welded Random CNT Network Structures. *Int. J. Hydrogen Energy* **2015**, *40*, 403–411.
- (66) Wu, C.-D.; Fang, T.-H.; Lo, J.-Y. Effects of Pressure, Temperature, and Geometric Structure of Pillared Graphene on Hydrogen Storage Capacity. *Int. J. Hydrogen Energy* **2012**, *37*, 14211–14216.
- (67) Leach, A. R. *Molecular modeling: Principles and applications*; Pearson Prentice Hall, 2001.
- (68) Henkelman, G.; Arnaldsson, A.; Jónsson, H. A Fast and Robust Algorithm for Bader Decomposition of Charge Density. *Comput. Mater. Sci.* **2006**, *36*, 354–360.
- (69) Ryan, P.; Farha, O. K.; Broadbelt, L. J.; Snurr, R. Q. Computational Screening of Metal-Organic Frameworks for Xenon/krypton Separation. *AIChE J.* **2011**, *57*, 1759–1766.
- (70) Rai, N.; Wagner, A. J.; Ross, R. B.; Siepmann, J. I. Application of the TraPPE Force Field for Predicting the Hildebrand Solubility Parameters of Organic Solvents and Monomer Units. *J. Chem. Theory Comput.* **2008**, *4*, 136–144.
- (71) Myers, A.; Monson, P. Adsorption in Porous Materials at High Pressure: Theory and Experiment. *Langmuir* **2002**, *18*, 10261–10273.
- (72) Nicholson, D.; Parsonage, N. G. Computer Simulation and the Statistical Mechanics of Adsorption. (*No Title*) **1982**.
- (73) Fjermestad, T.; Li, W.-q.; Rugg, G.; Ishida, S.; Okuno, M.; Sagi, K.; Genest, A.; Rösch, N. Acrolein Oxidation to Acrylic Acid Over the MoVO_x Material. Insights From DFT Modeling. *Appl. Catal. A Gen.* **2018**, *565*, 68–75.
- (74) Ishikawa, S.; Kobayashi, D.; Konya, T.; Ohmura, S.; Murayama, T.; Yasuda, N.; Sadakane, M.; Ueda, W. Redox Treatment of Orthorhombic Mo₂Nv₁₁O₁₂ and Relationships Between Crystal Structure, Microporosity and Catalytic Performance for Selective Oxidation of Ethane. *The Journal of Physical Chemistry C* **2015**, *119*, 7195–7206.
- (75) Ishikawa, S.; Zhang, Z.; Murayama, T.; Hiyoshi, N.; Sadakane, M.; Ueda, W. Multi-Dimensional Crystal Structuring of Complex Metal Oxide Catalysts of Group V and VI Elements by Unit-Assembling. *Top. Catal.* **2019**, *62*, 1157–1168.
- (76) Ishikawa, S.; Zhang, Z.; Ueda, W. Unit Synthesis Approach for Creating High Dimensionally Structured Complex Metal Oxides as Catalysts for Selective Oxidations. *ACS Catal.* **2018**, *8*, 2935–2943.
- (77) Sadakane, M.; Kodato, K.; Kuranishi, T.; Nodasaka, Y.; Sugawara, K.; Sakaguchi, N.; Nagai, T.; Matsui, Y.; Ueda, W. Molybdenum–Vanadium-Based Molecular Sieves with Microchannels of Seven-Membered Rings of Corner-Sharing Metal Oxide Octahedra. *Angew. Chem. Int. Ed.* **2008**, *47*, 2493–2496.
- (78) Lunkenbein, T.; Girgsdies, F.; Wernbacher, A.; Noack, J.; Auferrmann, G.; Yasuhara, A.; Klein-Hoffmann, A.; Ueda, W.; Eichelbaum, M.; Trunschke, A.; Schlögl, R.; Willinger, M. G. Direct Imaging of Octahedral Distortion in a Complex Molybdenum Vanadium Mixed Oxide. *Angew. Chem. Int. Ed.* **2015**, *54*, 6828–6831.
- (79) Grasselli, R. K.; Volpe, A. F. Catalytic Consequences of a Revised Distribution of Key Elements at the Active Centers of the M1 Phase of the MoVNbTeO X System. *Top. Catal.* **2014**, *57*, 1124–1137.
- (80) Li, W.-Q.; Fjermestad, T.; Genest, A.; Rösch, N. Reactivity Trends of the MoVO X Mixed Metal Oxide Catalyst From Density Functional Modeling. *Catal. Sci. Technol.* **2019**, *9*, 1559–1569.
- (81) Arce-Ramos, J. M.; Genest, A.; Rösch, N. How TeO Defects in the MoVNbTeO Catalyst Material Affect the V⁴⁺ Distribution: A Computational Study. *J. Phys. Chem. C* **2020**, *124*, 18628–18638.
- (82) Cheng, M.-J.; Goddard III, W. A. In Silico Design of Highly Selective Mo–V–Te–Nb–O Mixed Metal Oxide Catalysts for Ammonoxidation and Oxidative Dehydrogenation of Propane and Ethane. *J. Am. Chem. Soc.* **2015**, *137*, 13224–13227.
- (83) Willinger, M. G. Direct Imaging of Octahedral Distortion in a Complex Molybdenum Vanadium Mixed Oxide. Symposium on Advanced Materials Analysis by latest STEM Technologies, Max-Planck-Institut für Kohlenforschung.
- (84) DeSanto, P.; Buttrey, D. J.; Grasselli, R. K.; Lugmair, C. G.; Volpe, A. F.; Toby, B. H.; Vogt, T. Structural Characterization of the Orthorhombic Phase M1 in MoVNbTeO Propane Ammonoxidation Catalyst. *Top. Catal.* **2003**, *23*, 23–38.
- (85) DeSanto Jr, P.; Buttrey, D. J.; Grasselli, R. K.; Lugmair, C. G.; Volpe Jr, A. F.; Toby, B. H.; Vogt, T. Structural Aspects of the M1 and M2 Phases in MoVNbTeO Propane Ammonoxidation Catalysts. *Zeitschrift für Kristallographie-Crystalline Materials* **2004**, *219*, 152–165.
- (86) Li, X.; Buttrey, D. J.; Blom, D. A.; Vogt, T. Improvement of the Structural Model for the M1 Phase Mo–V–Nb–Te–O Propane (Amm) Oxidation Catalyst. *Top. Catal.* **2011**, *54*, 614–626.
- (87) Epicier, T.; Aouine, M.; Nguyen, T. T.; Millet, J.-M. M. Spatial Distribution of the Vanadium Atomic Species in MoVTeO and MoVTeNbO Oxide Catalysts as Revealed by High-Angle Annular Dark-Field Scanning Transmission Electron Microscopy. *Chem. Cat. Chem.* **2017**, *9*, 3526–3533.
- (88) Jahn, H. A.; Teller, E. Stability of Polyatomic Molecules in Degenerate Electronic States—I—Orbital Degeneracy. *P. Roy. Soc. Lond. A Mat.* **1937**, *161*, 220–235.
- (89) Raabe, J.-C.; Jameel, F.; Stein, M.; Albert, J.; Poller, M. J. Heteroelements in Polyoxometalates: a Study on the Influence of Different Group 15 Elements on Polyoxometalate Formation. *Dalton Trans.* **2024**, *53*, 454–466.
- (90) Eason, T. L.; Moreau, F.; Yan, Y.; Yang, S.; Schröder, M. Structural and Dynamic Studies of Substrate Binding in Porous Metal-Organic Frameworks. *Chem. Soc. Rev.* **2017**, *46*, 239–274.
- (91) Wang, H.; Lustig, W. P.; Li, J. Sensing and Capture of Toxic and Hazardous Gases and Vapors by Metal-Organic Frameworks. *Chem. Soc. Rev.* **2018**, *47*, 4729–4756.
- (92) Zhao, X.; Wang, Y.; Li, D.-S.; Bu, X.; Feng, P. Metal-Organic Frameworks for Separation. *Adv. Mater.* **2018**, *30*, 1705189.

- (93) Banerjee, D.; Simon, C. M.; Plonka, A. M.; Motkuri, R. K.; Liu, J.; Chen, X.; Smit, B.; Parise, J. B.; Haranczyk, M.; Thallapally, P. K. Metal-Organic Framework with Optimally Selective Xenon Adsorption and Separation. *Nat. Commun.* **2016**, *7*, 1–7.
- (94) Gong, Y.; Tang, Y.; Mao, Z.; Wu, X.; Liu, Q.; Hu, S.; Xiong, S.; Wang, X. Metal-Organic Framework Derived Nanoporous Carbons with Highly Selective Adsorption and Separation of Xenon. *J. Mater. Chem. A* **2018**, *6*, 13696–13704.
- (95) Fernandez, C. A.; Liu, J.; Thallapally, P. K.; Strachan, D. M. Switching Kr/Xe Selectivity with Temperature in a Metal-Organic Framework. *J. Am. Chem. Soc.* **2012**, *134*, 9046–9049.
- (96) Xiong, X.-l.; Chen, G.-h.; Xiao, S.-t.; Ouyang, Y.-g.; Li, H.-b.; Wang, Q. New Discovery of Metal-Organic Framework UTSA-280: Ultrahigh Adsorption Selectivity of Krypton Over Xenon. *J. Phys. Chem. C* **2020**, *124*, 14603–14612.
- (97) Boerner, T. J.; Deems, S.; Furlani, T. R.; Knuth, S. L.; Towns, J. ACCESS: Advancing Innovation: NSF’s Advanced Cyberinfrastructure Coordination Ecosystem: Services & Support. Practice and Experience in Advanced Research Computing. New York, NY, USA, 2023; pp 173–176.